# Shipboard Wave Measurements in the Southern Ocean

BJÖRN LUND

*Rosenstiel School of Marine and Atmospheric Science, University of Miami, Miami, Florida*

CHRISTOPHER J. ZAPPA

*Lamont-Doherty Earth Observatory, Columbia University, Palisades, New York*

HANS C. GRABER

*Rosenstiel School of Marine and Atmospheric Science, University of Miami, Miami, Florida*

ALEJANDRO CIFUENTES-LORENZEN

*University of Connecticut, Storrs, Connecticut*

(Manuscript received 27 October 2016, in final form 7 July 2017)

ABSTRACT

Surface wave measurements from ships pose difficulties because of motion contamination. Cifuentes-Lorenzen et al. analyzed laser altimeter and marine X-band radar (MR) wave measurements from the Southern Ocean Gas Exchange Experiment (SOGasEx). They found that wave measurements from both sensors deteriorate precipitously at ship speeds $> 3\,\mathrm{m\,s^{-1}}$. This study demonstrates that MR can yield accurate wave frequency–direction spectra independent of ship motion. It is based on the same shipborne SOGasEx wave data but uses the MR wave retrieval method proposed by Lund et al. and a novel empirical transfer function (ETF). The ETF eliminates biases in the MR wave spectra by redistributing energy from low to high frequencies. The resulting MR wave frequency–direction spectra are shown to agree well with laser altimeter wave frequency spectra from times when the ship was near stationary and with WAVEWATCH III (WW3) model wave parameters over the full study period.

## 1. Introduction

The Southern Ocean is particularly sensitive to climate change, as evidenced by its rapidly rising heat content (e.g., Gille 2002). This and other changes to the Southern Ocean climate are dependent on the exchange of energy, mass, and momentum across the interface between ocean and atmosphere (and ice, if present) (Sprintall et al. 2012). Yet, air–sea flux magnitudes and variations in the Southern Ocean are still poorly known (Sahlée et al. 2012). The wave climate of the Southern Ocean is similarly understudied (Hemer et al. 2010). Existing studies have mainly focused on the Northern Hemisphere, which is more relevant to shipping (e.g., Swail and Cox 2000). Waves are known to affect the air–sea momentum and gas exchange (Donelan et al. 1993; Zappa et al. 2001, 2004; Högström et al. 2015). The Southern Ocean is characterized by frequent storms with practically unlimited fetch, resulting in typically swell-dominated seas with high significant wave heights (Young 1999). The lack of in situ air–sea flux and wave data for the Southern Ocean is largely owing to the difficulties associated with making high-latitude measurements (Bourassa et al. 2013). Routine shipboard wave measurements could help reduce this dearth of observations.

This study presents marine X-band radar (MR) wave frequency–direction spectra that were acquired from R/V *Ronald H. Brown* during the Southern Ocean Gas Exchange Experiment (SOGasEx; Ho et al. 2011). Measuring waves from ships is challenging because of the platform motion. Past studies have used a combination of wave staffs and shipboard inertial measurement units (IMUs) to measure waves

*Corresponding author*: Björn Lund, blund@rsmas.miami.edu

DOI: 10.1175/JTECH-D-16-0212.1

© 2017 American Meteorological Society. For information regarding reuse of this content and general copyright information, consult the AMS Copyright Policy (www.ametsoc.org/PUBSReuseLicenses).

Brought to you by NOAA Central Library | Unauthenticated | Downloaded 01/16/24 07:13 PM UTC

from ships (Drennan et al. 1994; Hanson et al. 1997). Others have analyzed ship motion data in the same manner as measurements from a surface following wave buoy, assuming a linear transfer function from ship response to wave spectrum (e.g., Nielsen and Stredulinsky 2012; Collins et al. 2015). The ship-motion-induced Doppler effect redistributes wave energy over frequency and is difficult to correct, especially if the wave direction relative to the direction of ship motion is unknown (Lindgren et al. 1999; Collins et al. 2016).

More recently, it has been proposed to measure waves from ships by combining MR with IMU (Stredulinsky and Thornhill 2011) and laser altimeter (Cifuentes-Lorenzen et al. 2013) data. Both studies suggest that MR provides a good peak wave direction and period but unreliable significant wave height. For better results, the MR wave frequency–direction spectra must be scaled using significant wave heights from an altimeter (which is preferable over IMU measurements alone, since no transfer function is required). Nevertheless, Cifuentes-Lorenzen et al. (2013) find that this technique yields adequate wave measurements only if the ship speed over ground (SOG) is $<3\,\mathrm{m\,s^{-1}}$. This view has been challenged by Lund et al. (2016), who introduced a novel underway shipboard MR wave retrieval method. Their study is based on ~26 days of MR measurements from the western Pacific and focuses on the multidirectional wave characteristics. It uses buoy and model data to show that accurate MR wave frequency–direction spectra can be obtained independent of ship motion. However, they do observe that the MR mean period is biased high, which they attribute to imperfections in the standard modulation transfer function (MTF; see Nieto Borge et al. 2004) converting the MR image into wave spectra.

This study continues where Lund et al. (2016) left off, shifting the focus from the directional to the frequency distribution of wave energy. It is demonstrated that the Lund et al. (2016) method, which is based on the pioneering studies of Young et al. (1985) and Nieto Borge et al. (2004), yields wave frequency–direction spectra that are accurate near the spectral peak, but overestimates the low-frequency energy and underestimates the high-frequency energy. To avoid the Doppler correction issues mentioned above, we focus on periods when the ship was near stationary. The corresponding collocated MR and laser altimeter wave frequency spectra are split into a ''training'' dataset and a ''testing'' dataset. A novel empirical transfer function (ETF) is defined based on the training data. The bias-corrected MR wave spectra from both the training and testing data are in good agreement with the laser altimeter measurements as well as with the model results.

This paper is organized as follows: Section 2 provides an overview of the MR, laser altimeter, and model data used. Section 3 briefly revisits the MR and laser altimeter methodologies used for measuring waves. Results are presented in section 4, which is followed by a discussion (section 5) and conclusions (section 6).

## 2. Data overview

SOGasEx 2008 was the third in a series of U.S.-led studies that aimed at improving our understanding of air–sea gas exchange processes. It was motivated by the importance of the Southern Ocean for the global climate system. The experiment was conducted from *Ronald H. Brown* and took place in the Southern Ocean's southwestern sector of the Atlantic, north of the island of South Georgia, during the austral fall of 2008. It focused around two tracer releases and their subsequent sampling. These efforts were complemented by extensive measurements of the upper ocean and marine air to quantify air–sea fluxes (Ho et al. 2011; Sahlée et al. 2012).

During SOGasEx a science MR was installed approximately 20 m ASL on top of the wheelhouse of *Ronald H. Brown* (see Fig. 1a). It is based on a standard Furuno X-band (9.4 GHz) MR with an 8-ft horizontally polarized antenna, as typically used for navigation. The MR was connected to a wave monitoring system (WaMoS), consisting of a desktop computer with a radar data acquisition board, wave retrieval software, and a screen for displaying results (Dittmer 1995; Ziemer 1995). The WaMoS was operated continuously throughout the experiment, sampling the raw MR backscatter intensity from the sea surface. The MR data analyzed here were collected over a 1-month period from 5 March to 5 April 2008. The data have frequent gaps, although typically short (<1 h), because of data acquisition issues. A map with the corresponding cruise track is shown in Fig. 2.

The SOGasEx MR backscatter intensity images have a maximum range of ~2.1 km, a range resolution of 7.5 m, a 12-bit gray-level depth (note that the radar return was not radiometrically calibrated), and were updated every 1.5 s (the antenna rotation period). To achieve such a fine range resolution, the system was set to operate in short-pulse mode (pulse length of 50 ns). In this mode the MR has a pulse repetition frequency of 3 kHz, but because of hardware limitations WaMoS sampled only approximately every other radar pulse. Figure 3 gives a radar image example from 0200 UTC 11 March 2008. The

Brought to you by NOAA Central Library | Unauthenticated | Downloaded 01/16/24 07:13 PM UTC

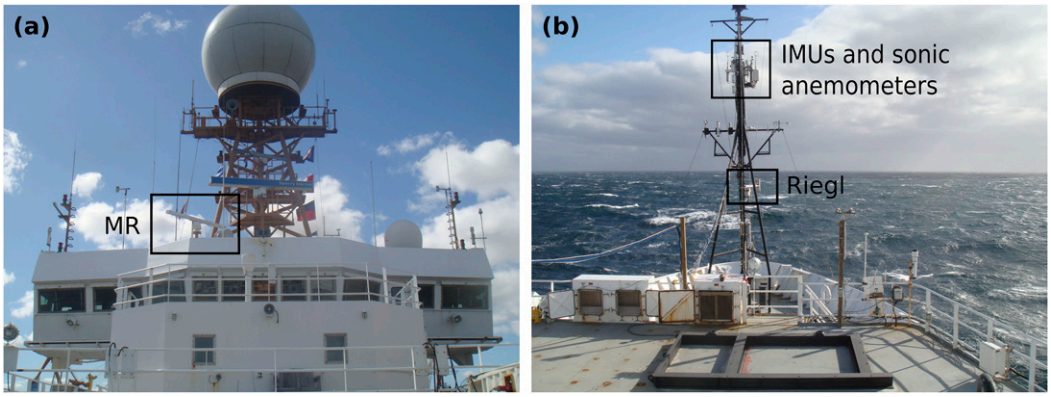


FIG. 1. (a) Picture of the Furuno science MR on top of the wheelhouse of R/V *Ronald H. Brown*. (b) Picture of the Riegl laser altimeter, IMUs, and sonic anemometers on the jack staff of *Ronald H. Brown*. (Photo credit: Alejandro Cifuentes-Lorenzen.)

radar image shows waves coming from the west-southwest. A small portion of the radar field of view (FOV; from south to south-southwest) is shadowed by the ship's main mast.

To complement the MR data, this study uses Riegl LD90-3800VHS-FLP laser altimeter measurements. During SOGasEx the Riegl system was installed 10 m ASL on the jack staff at the bow of the ship (see Fig. 1b). To clear the bow of the ship, it was deployed with a 15° incidence angle, which sets the Riegl beam 7.85 m in front of the waterline. It yields the instantaneous distance to the sea surface at a frequency of 10 Hz with a 2.65-cm footprint for a 10-m range. The measurement accuracy is ±50 mm (Riegl 2010).

This study furthermore consults WAVEWATCH III (WW3) peak and integral wave parameters from the global hindcast database of the French

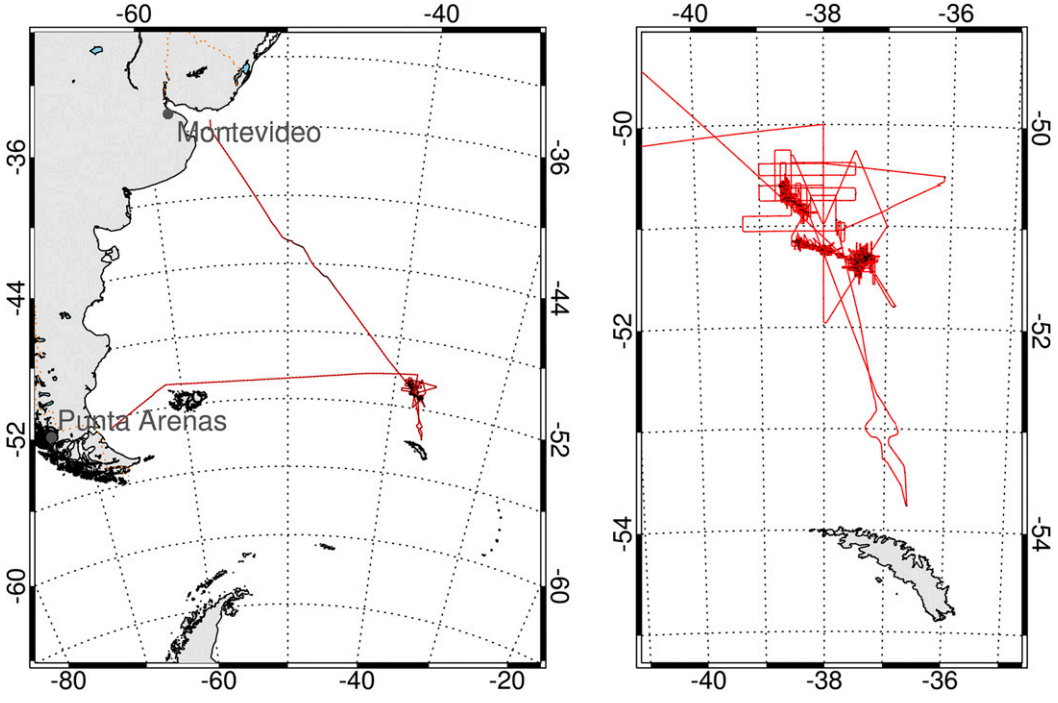


FIG. 2. (left) Map of *Ronald H. Brown* SOGasEx cruise from Punta Arenas, Chile, to Montevideo, Uruguay. (right) Close-up of cruise track during the 1-month experiment north of the island of South Georgia.

Brought to you by NOAA Central Library | Unauthenticated | Downloaded 01/16/24 07:13 PM UTC

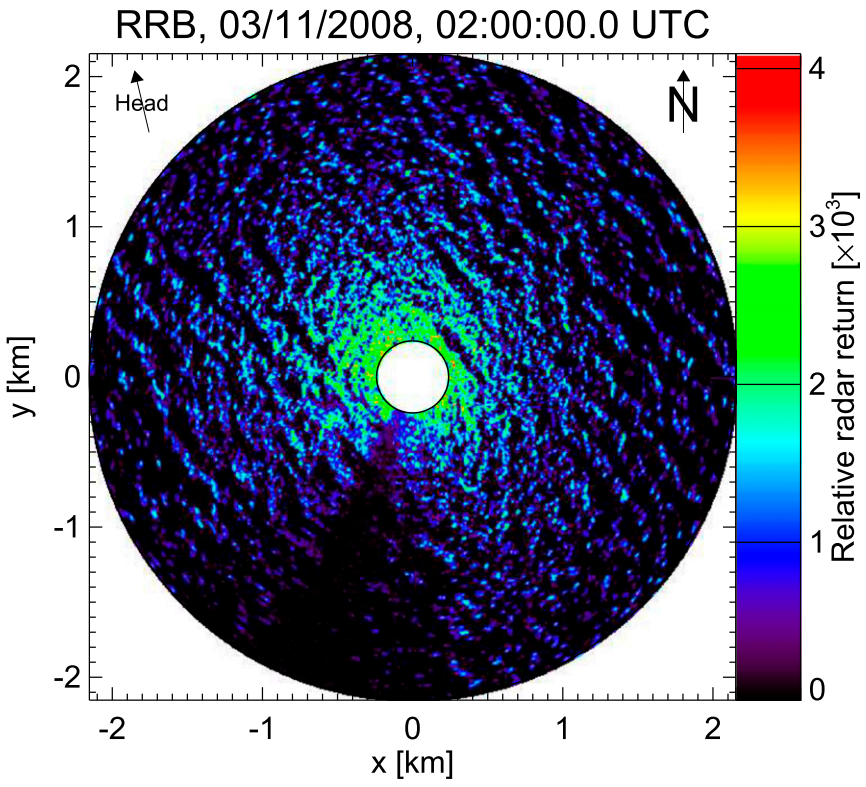


FIG. 3. MR backscatter intensity image acquired from *Ronald H. Brown* on 0200 UTC 11 Mar 2008.

Research Institute for Exploitation of the Sea [Institut Français de Recherche pour l'Exploitation de la Mer (IFREMER)].[1] The hindcast was performed on a global grid with a 0.5° spatial resolution and a 3-hourly temporal resolution. Wave parameters were computed for frequencies up to $0.72\,s^{-1}$. The model run used here is based on winds from ECMWF analyses and ST4-TEST471 source term parameterizations (Rascle and Ardhuin 2013). In addition, this study uses 10-m neutral winds from a flux package that was installed on top of the jack staff (18 m ASL; see Fig. 1b). The flux package includes two IMUs (Systron Donner MotionPak 6-variable) and three Gill R-3 sonic anemometers.

## 3. Methodology

### a. Marine X-band radar

The MR backscatter from the sea surface is controlled by centimeter-scale roughness elements, as explained by Bragg scattering theory (among other mechanisms) (Wright 1968). The hydrodynamic modulation, tilt modulation, and shadowing associated with ocean waves result in a prominent radar signal (Nieto Borge et al. 2004). The wave signal obeys the linear dispersion relationship

$$\omega = \pm\sqrt{gk\tanh kh} + \mathbf{k}\cdot\mathbf{U}, \tag{1}$$

with the angular frequency $\omega$, the wavenumber $k = |\mathbf{k}|$, the acceleration as a result of gravity $g$, the water depth $h$, and the current velocity $\mathbf{U}$.

The MR wave retrieval method employed here is based on the standard approach by Young et al. (1985), Senet et al. (2001), and Nieto Borge et al. (2004). After converting the raw polar radar data to Cartesian coordinates, a three-dimensional (3D) fast Fourier transform (FFT) is used to obtain the image wavenumber–frequency spectrum $F_I(\mathbf{k}, \omega)$. In deviation from the standard method, the 3D FFT is performed over the whole radar FOV, to address issues raised by Lund et al. (2014), and the radar signal is georeferenced on a pulse-by-pulse basis (Lund et al. 2015b). The wave energy, which gets Doppler shifted in presence of a near-surface current, is located on the so-called dispersion shell [Eq. (1)]. A near-surface current estimate is obtained using an

[1] See ftp://ftp.ifremer.fr/ifremer/ww3/HINDCAST/GLOBAL/2008_ECMWF/.

Brought to you by NOAA Central Library | Unauthenticated | Downloaded 01/16/24 07:13 PM UTC

iterative least squares fit, where select spectral coordinates are attributed to the sea state (Senet et al. 2001; Lund et al. 2015b). Here, the near-surface current estimates were "calibrated" in accordance with Lund et al. (2015a).

To remove most of the energy that is unrelated to the sea state, spectral components outside of the dispersion shell are set to zero, yielding the filtered spectrum $F_F(\mathbf{k}, \omega)$. Following Lund et al. (2016, 2015b), the background noise is estimated empirically and subtracted from the remaining spectral coordinates. The power in $F_F(\mathbf{k}, \omega)$ can thus be fully attributed to the wave field. The MTF $\mathscr{M}(k) = k^{-1.2}$ proposed by Nieto Borge et al. (2004) is applied to obtain the surface wave spectrum

$$F_W(\mathbf{k}, \omega) = F_F(\mathbf{k}, \omega)\,\mathscr{M}(k). \tag{2}$$

Integrating $F_W(\mathbf{k}, \omega)$ over frequencies yields the wavenumber spectrum

$$F(\mathbf{k}) = \int_{\omega_{\text{th}}}^{\omega_{\text{Ny}}} F_W(\mathbf{k}, \omega)\, d\omega, \tag{3}$$

where $\omega_{\text{th}}$ is a low-frequency threshold and $\omega_{\text{Ny}}$ is the Nyquist frequency.

For easier comparison with the laser altimeter measurements, $F(\mathbf{k})$ is converted to the frequency–direction spectrum

$$E(f, \theta) = F_W(\mathbf{k})\, k \frac{dk}{d\omega}. \tag{4}$$

The frequency spectrum

$$E(f) = \int_0^{2\pi} E(f, \theta)\, d\theta \tag{5}$$

yields the peak wave period $T_p = 1/f_p$, where $f_p = \max_f[E(f)]$, and the mean period $T_{m01} = m_0/m_1$, where $m_0$ is the spectrum's zeroth and $m_1$ is its first moment. The peak wave direction is given by $\theta_p = \theta_m(f_p)$, where $\theta_m(f_p) = \tan^{-1} b_1(f)/a_1(f)$ with $a_1(f)$ and $b_1(f)$ corresponding to the first pair of Fourier coefficients, which are computed from $E(f, \theta)$ (Hauser et al. 2005).

Significant wave height $H_s$ estimates are based on the signal-to-noise ratio (SNR; i.e., the ratio between the wave and background noise spectral components) in $F_I(\mathbf{k}, \omega)$ with

$$H_s = a + b\sqrt{\text{SNR}}, \tag{6}$$

where $a$ and $b$ are calibration constants. MR wave spectra are scaled such that $H_s = 4\sqrt{m_0}$ (Nieto Borge et al. 2008).

For further details on the wave retrieval method used here, refer to Lund et al. (2016). In this study, MR frequency–direction spectra and their corresponding wave parameters were produced using 10-min analysis periods covering the full 1-month experiment.

### b. Laser altimeter

The Riegl laser altimeter data were converted from a platform to a fixed frame of reference using the flux package's two IMUs. The result of this transformation is a time series of sea surface elevation; for details refer to Cifuentes-Lorenzen et al. (2013). To avoid correcting for the ship-motion-induced Doppler effect, the Riegl data were limited to periods during which *Ronald H. Brown* was near stationary, that is, ship SOG $< 1.5\,\text{m s}^{-1}$ (in contrast, MR wave frequency–direction spectra were produced at all ship speeds for the full 1-month period). The corresponding data were subdivided into blocks of 20 min. When the ship was stationary over longer periods, neighboring blocks were allowed to overlap by 10 min. A Blackman–Harris window was applied to each block and linear trends were removed. The wave frequency spectrum $E(f)$ was then computed for each time series via FFT (e.g., Björkqvist et al. 2016). Each spectrum was averaged over 10 frequency bins in order to improve the signal-to-noise ratio. This data selection and processing resulted in 998 Riegl wave frequency spectra (and 868 MR–Riegl data pairs) that can be used for this study. Wave parameters $T_p$, $T_{m01}$, and $H_s$ were computed from $E(f)$ as detailed in the previous subsection. To avoid ship-induced shadowing effects, the Riegl data were further limited to periods when the relative direction between ship heading and MR $\theta_p$ was within ±90°. This led to the dismissal of 54 Riegl spectra, leaving 814 MR–Riegl data pairs for this study.

## 4. Results

### a. Significant wave height calibration

Reference $H_s$ measurements are needed to define the MR $H_s$ calibration constants [see Eq. (6)]. Here, the Riegl laser altimeter measurements (limited to periods of near stationarity, as in the following subsections) constitute an excellent reference dataset. Figure 4 shows the MR $\sqrt{\text{SNR}}$ plotted against the Riegl $H_s$. The linear best fit between these two variables yields the calibration constants (here, $a = -1.96$ and $b = 2.63$). The calibration is based on 272 MR–Riegl measurement pairs that were set aside for training. The training data include all MR–Riegl pairs starting from 1100 UTC 25 March 2008. The remaining 542 MR–Riegl pairs (starting from the beginning of this study) will be used for testing, that

Brought to you by NOAA Central Library | Unauthenticated | Downloaded 01/16/24 07:13 PM UTC

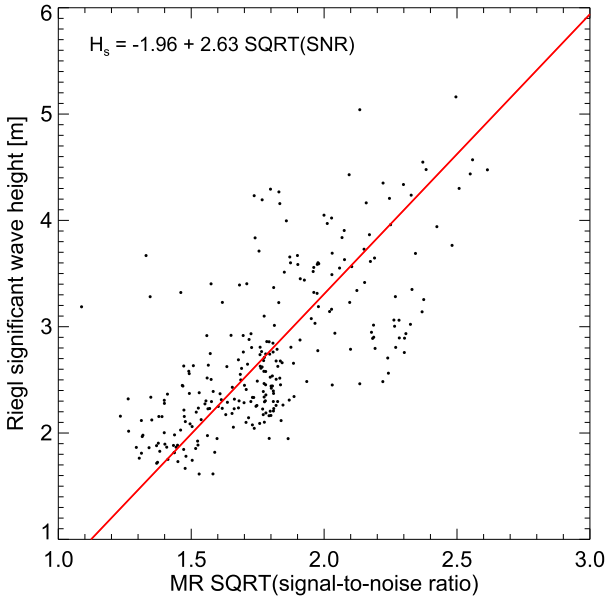


FIG. 4. Scatterplot of the MR $\sqrt{\text{SNR}}$ against the Riegl $H_s$ from the training data. MR $H_s$ calibration function shown in the top-left corner is based on the linear best fit (red line).

is, to assess the $H_s$ calibration constants' validity outside of the training period.

### b. *Empirical transfer function*

A recent study by Lund et al. (2016) investigated the multidirectional characteristics of shipboard MR wave frequency–direction spectra from the western Pacific. They used the MTF from Nieto Borge et al. (2004), which simply assumes the ratio between the radar image and the wave wavenumber–frequency spectrum to be proportional to $k^{1.2}$ [see Eq. (2)]. The resulting MR frequency–direction spectra were accurate in terms of $T_p$ (and other parameters), but $T_{m01}$ was biased high. This study aims to improve our understanding of this bias and to develop a means of correcting for it.

For consistency with Lund et al. (2016) and earlier studies (e.g., Hessner et al. 2008), the $F_F(\mathbf{k}, \omega)$ from SOGasEx were transformed to surface wave spectra using the same $k^{1.2}$ proportionality [see Eq. (2)]. They were subsequently converted to wave frequency spectra according to Eqs. (3)–(5), and then scaled to have the correct $H_s$ based on the SNR and the calibration constants from the previous subsection [see Eq. (6)].

Figure 5 shows the ratio between the 272 pairs of Riegl and MR wave frequency spectra that make up the training dataset (see the previous subsection). The spectral ratio is shown on a logarithmic scale with the color code corresponding to the Riegl $T_{m01}$. All MR frequency spectra exhibit a similar trend: they overestimate the wave energy at the low frequencies and underestimate the high-frequency energy. These effects are most pronounced on either end of the spectrum. This is bound to result in an MR $T_{m01}$ that is biased high, as already observed by Lund et al. (2016) (for a different dataset). This result indicates that the Nieto Borge et al. (2004) MTF is insufficient at the very low ($<0.05^{-1}$) and high ($>0.2^{-1}$) frequencies. Furthermore, the low- and high-frequency biases appear to be independent of $T_{m01}$ (as well as $T_p$ and $H_s$, not shown).

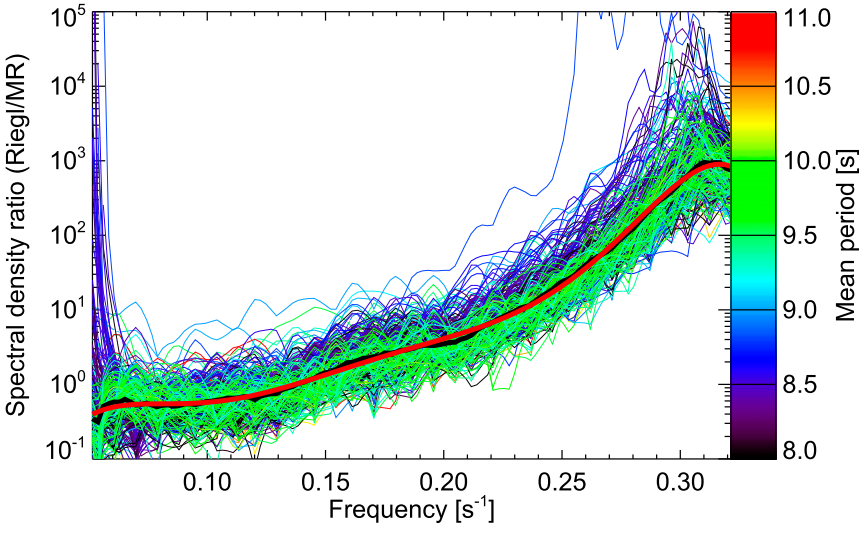


FIG. 5. ETF for correcting the MR wave spectra's frequency distribution of energy, based on the training data. Ratio between the Riegl and MR wave frequency spectra (thin curve), with the color code indicating the Riegl $T_{m01}$; median ratio (thick black curve); and sixth-order polynomial best-fit curve (thick red curve).

Brought to you by NOAA Central Library | Unauthenticated | Downloaded 01/16/24 07:13 PM UTC

The figure also includes the median energy density ratio at each frequency (thick red curve) and the corresponding sixth-order polynomial fit (thick black curve), which is given by

$$\log_{10}\mathcal{T}(f) = -5.26 + 236.72f - 4393.09f^2 + 40\,409.45f^3 - 193\,246.30f^4 + 462\,735.06f^5 - 436\,029.55f^6.$$

In the following, $\mathcal{T}(f)$ will serve as ETF yielding bias-corrected MR wave frequency spectra:

$$E_{\mathrm{BC}}(f,\theta) = E(f,\theta)\mathcal{T}(f). \quad (7)$$

The ETF is valid over the frequency range covered by the MR ($\sim$0.05–0.32 $\mathrm{s}^{-1}$). The MR–Riegl testing data (542 pairs of spectra, as defined in the previous subsection) will be used to assess the ETF's performance with data it had not "seen" before.

The bias-corrected MR spectra (rescaled to preserve $H_s$) and the corresponding Riegl wave frequency spectra are shown as time series in Fig. 6. The results are shown separately for the training and testing data (note that the time series cover the full study period but have extensive gaps, since the Riegl data were limited to periods of near stationarity). Spectral densities are displayed on a logarithmic scale. The MR training and testing data are in good qualitative agreement with the Riegl measurements. They show the same features throughout the study period, including prominent dual peaks (indicative of multimodal seas) on several occasions (e.g., around spectrum numbers 110 and 500 in the training and testing data, respectively).

Figure 7 gives examples of MR wave frequency spectra before and after bias correction as well as the corresponding Riegl reference spectra. The spectra are presented on a log–log scale. The figure covers a broad range of wave conditions and spans the entire study period, with Figs. 7a–e stemming from the testing dataset and Figs. 7f–i stemming from the training dataset. The Riegl and bias-corrected MR spectra from both datasets are in good agreement. They frequently exhibit multiple or broad peaks that are indicative of mixed seas. The differences between the bias-corrected and the original MR spectra are most pronounced at the high-frequency tail ($>\sim$0.2 $\mathrm{s}^{-1}$). The figure includes the $f^{-4}$ slope of the equilibrium range for reference (Donelan et al. 1985). Both the Riegl and the bias-corrected MR spectra exhibit an $f^{-4}$ decay, whereas the uncorrected MR spectra's slope is much steeper.

There are exceptions to the good MR–Riegl agreement. Figure 8 presents three examples where the MR and Riegl wave frequency spectra are in relatively poor agreement. In Fig. 8a the MR high-frequency energy (around 0.3 $\mathrm{s}^{-1}$) deviates sharply from the Riegl reference measurements. The observed dip in the MR spectral density can be explained by rain or fog, which tends to obscure the wave signal at the higher frequencies. This is because the high-frequency signal is generally only slightly above the background noise level. In Fig. 8b the Riegl peak period is exceptionally long at $\sim$16 s. For this case, the bias-corrected MR spectrum underestimates the low-frequency energy. Last, Fig. 8c gives an example where the Riegl reported a spurious increase in the low-frequency energy (from $\sim$0.07 $\mathrm{s}^{-1}$ to the lower-frequency limit). The Riegl wave frequency spectra acquired directly before and after are in good agreement with the MR spectra (not shown).

### c. Peak wave parameters

Figure 9 shows a time series of peak and integral wave parameters for MR, Riegl, and WW3. In addition, it shows the corresponding 10-m neutral wind speed and direction from the flux package as well as SOG and heading. The WW3 wave parameters were bilinearly interpolated to match the track of *Ronald H. Brown*. The MR parameters are based on the bias-corrected wave frequency–direction spectra [see Eq. (7)]. The vertical dashed lines separate the testing and training datasets (see previous subsections). The MR and Riegl measurements as well as the WW3 model results are in good overall agreement. The sea state during the experiment was dominated by swells coming from the south to the northwest with a maximum $H_s$ of $\sim$5 m and $T_p$ values up to $\sim$16 s. The $H_s$ was generally $>$1 m and $T_p > 6$ s. The $T_p$ from all sources underwent frequent sudden changes, which happens when two (or more) wave systems with different peak frequencies have similar energy levels.

Riegl data are lacking during periods when the ship's SOG was $>$1.5 m $\mathrm{s}^{-1}$. To assess the MR wave parameter's sensitivity to ship motion, it helps to inspect the time series visually. The ship heading and speed changed frequently during SOGasEx (see Fig. 9's bottom two panels). But the MR wave parameters generally remain stable and do not exhibit sudden jumps, for example, when the ship picks up speed or changes heading. The high-frequency tails of the MR spectra from underway periods furthermore tend to follow the classic $f^{-4}$ slope, as they were observed to do during periods of near stationarity (see Fig. 7). Last, the statistical comparison of the MR and WW3 wave parameters yields comparable results for different ship speed brackets (in the interest of brevity, the last two points are not shown here). All evidence thus suggests that the MR wave frequency–direction spectra

Brought to you by NOAA Central Library | Unauthenticated | Downloaded 01/16/24 07:13 PM UTC

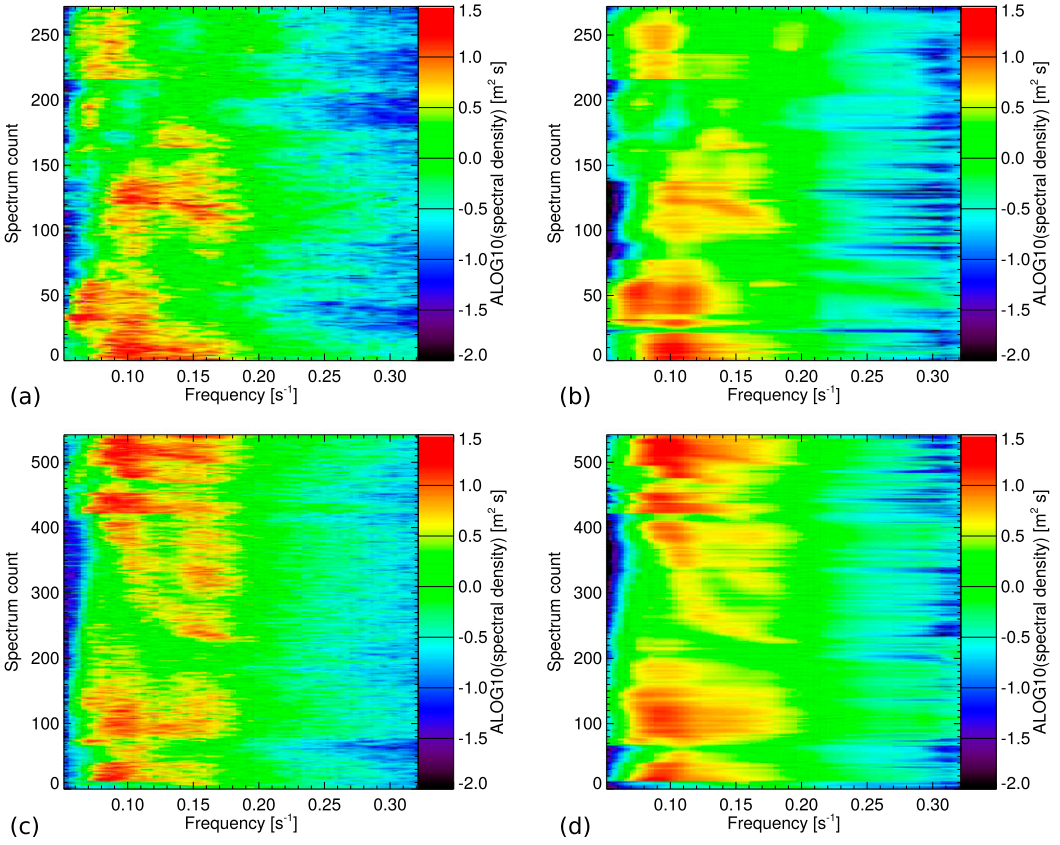


FIG. 6. (a) Riegl and (b) MR collocated wave frequency spectra from the training dataset as time series. (c) Riegl and (d) MR collocated wave frequency spectra from the testing dataset. Spectrum count is used to indicate time. Spectral density is shown on a logarithmic scale.

do not depend on ship motion, in concordance with Lund et al.'s (2016) findings for a different shipboard MR dataset (albeit with a focus on the waves' directional characteristics).

Figure 10 shows scatterplots of the pre-bias- and post-bias-correction MR $T_{m01}$ against the corresponding Riegl measurements for the testing and training data. The MR versus Riegl $T_{m01}$ measurements have an $r^2$ of 0.62, a bias of 0.16 s, and a $\sigma_{xy}$ of 0.39 s (for the testing data). These statistics represent a slight improvement over the training data. The ETF can thus be considered valid beyond the testing period. Without ETF both testing and training data exhibit a much more pronounced bias of ~2 s, demonstrating the ETF's effectiveness. Note that the WW3 $T_{m01}$ is biased high by ~1 s compared with both the Riegl and the (bias corrected) MR measurements. This is at least partially because WW3 wave spectra were not available for this study. Hence, the WW3 peak and integral wave parameters correspond to a much broader frequency range than the MR and Riegl parameters (both of which were computed over the MR frequency range).

The MR $H_s$ exhibits a few outliers that occurred during periods of heavy fog (e.g., on yearday 85). For the testing data, their statistical comparison with the Riegl $H_s$ measurements yields an $r^2$ of 0.64, a bias of 0.12 m, and a $\sigma_{xy}$ of 0.51 m. This result presents a slight improvement over the training dataset, suggesting that the $H_s$ calibration constants are generally applicable. Term $T_p$ has a large degree of natural variability, especially in the presence of multimodal seas, making it ill suited for statistical comparison. But it is worth mentioning that the Riegl $T_p$ measurements have significantly more scatter than the MR measurements. Table 1 summarizes the MR–Riegl peak and integral wave parameter comparison statistics for both training and testing data, including the $T_p$ and $T_{m01}$ statistics that would result if no ETF were applied.

## 5. Discussion

This study focuses on the distribution of MR wave energy over frequency. The simultaneous MR and Riegl laser altimeter measurements made from *Ronald H. Brown*

Brought to you by NOAA Central Library | Unauthenticated | Downloaded 01/16/24 07:13 PM UTC

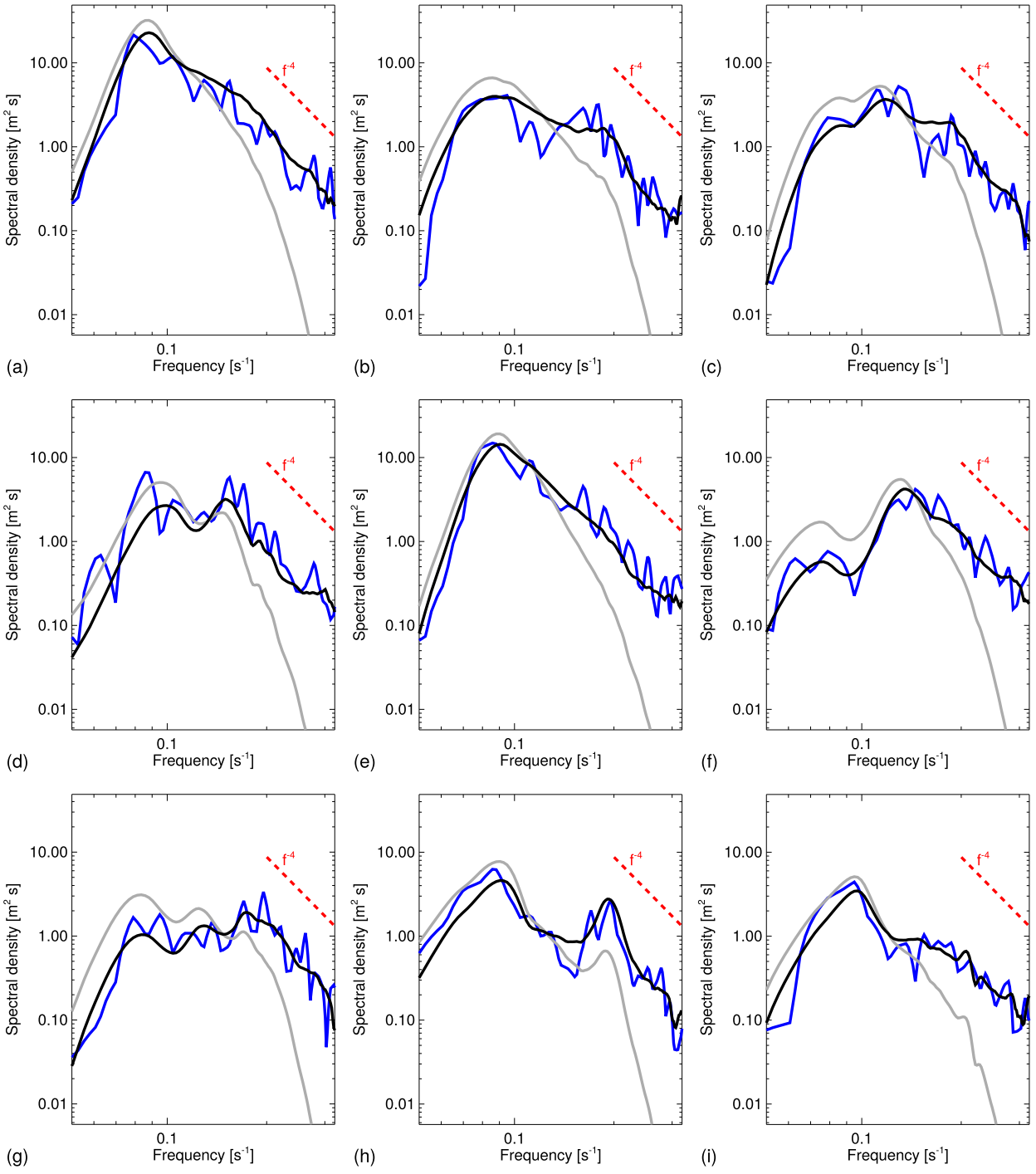


FIG. 7. Examples of Riegl (blue) and MR wave frequency spectra before (gray) and after (black) ETF correction. Spectra are plotted on a log–log scale. The $f^{-4}$ slope is indicated (red dashed line). Each MR and Riegl spectrum is based on 10 and 20 min of data, respectively. They were acquired at (a) 0310 UTC 11 Mar 2008, (b) 2235 UTC 15 Mar 2008, (c) 1130 UTC 16 Mar 2008, (d) 0725 UTC 18 Mar 2008, (e) 1210 UTC 21 Mar 2008, (f) 1900 UTC 31 Mar 2008, (g) 1330 UTC 2 Apr 2008, (h) 1305 UTC 4 Apr 2008, and (i) 0115 UTC 5 Apr 2008.

Brought to you by NOAA Central Library | Unauthenticated | Downloaded 01/16/24 07:13 PM UTC

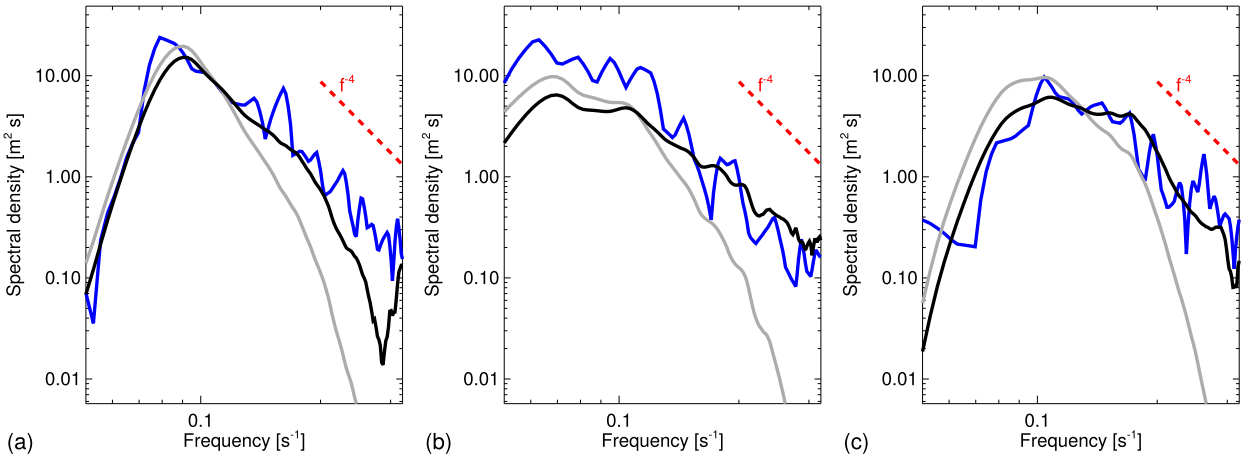


FIG. 8. As in Fig. 7, but showing examples of relatively poor MR–Riegl agreement that were acquired at (a) 0525 UTC 21 Mar 2008, (b) 0130 UTC 27 Mar 2008, and (c) 1500 UTC 29 Mar 2008.

during SOGasEx provide a unique opportunity to validate the MR wave frequency–direction spectra. The study's main finding is that the well-established MTF by Nieto Borge et al. (2004) overestimates the low-frequency and underestimates the high-frequency wave energy, as evidenced by a $T_{m01}$ that is biased high by ~2 s (compared with the Riegl measurements). An ETF has been defined to address this shortcoming. Given the challenges involved in making shipboard wave measurements, the bias-corrected MR wave frequency spectra are in good agreement with the Riegl reference data. For the testing dataset, the MR $T_{m01}$ bias has been reduced to 0.16 s after application of the ETF.

It is worthwhile noting that the Riegl wave frequency spectra (and $T_p$) exhibit significantly more scatter than the corresponding MR spectra (see Figs. 7 and 9). This can be explained by the fact that the Riegl measures the sea surface elevation at a single point, whereas the MR wave record is spatiotemporal. Hence, the MR samples a much larger number of waves per analysis period and has less statistical uncertainty (e.g., Gemmrich et al. 2016).

The MR and Riegl wave measurements were complemented by WW3 model results. The advantage of using a model is that results are available for the entire study period, whereas the Riegl measurements were limited to times when the ship was near stationary (to avoid Doppler correction issues). The WW3 $T_{m01}$ is biased high by ~1 s in both MR–WW3 and Riegl–WW3 comparisons, which may be explained by a broader frequency range in the model. This bias aside, the MR–WW3 and Riegl–WW3 comparisons indicate a similar level of agreement for $T_{m01}$, a better performance of the MR in terms of $T_p$, and a better performance of the Riegl regarding $H_s$. Furthermore, the model provides $\theta_p$ estimates, which are in excellent agreement with the MR measurements [see Lund et al. (2016) for an in-depth validation of the shipboard MR wave spectra's directionality]. The MR–WW3 comparison, which includes frequent periods during which the *Ronald H. Brown* was underway, suggests that the MR wave retrieval does not depend on ship motion.

Regarding the applicability of the ETF proposed here to other MR datasets, it should be noted that the MR wave retrieval method is a factor here. Using the standard wave retrieval method by Young et al. (1985), Senet et al. (2001), and Nieto Borge et al. (2004), it has been demonstrated that wave energy gets shifted from high to low frequencies with increasing range, which is likely due to shadowing (Lund et al. 2014). MR wave spectra furthermore depend on the relative angle between waves and antenna look directions. The MR retrieval methodology employed here counteracts these effects by analyzing the whole radar FOV. In addition, background noise contributions are subtracted from the filtered wavenumber–frequency spectra, which results in more realistic wave frequency–direction spectra, where all energy can be attributed to the waves (see section 3a). These deviations from the standard MR wave retrieval method are bound to affect the ETF, especially near the upper-frequency limit, where wave signal and background noise are of similar orders of magnitude.

## 6. Conclusions

It has been demonstrated by Lund et al. (2016) that one can retrieve highly accurate multidirectional wave characteristics from shipboard MR measurements. The research presented here complements their study by focusing on the frequency distribution of wave energy

Brought to you by NOAA Central Library | Unauthenticated | Downloaded 01/16/24 07:13 PM UTC

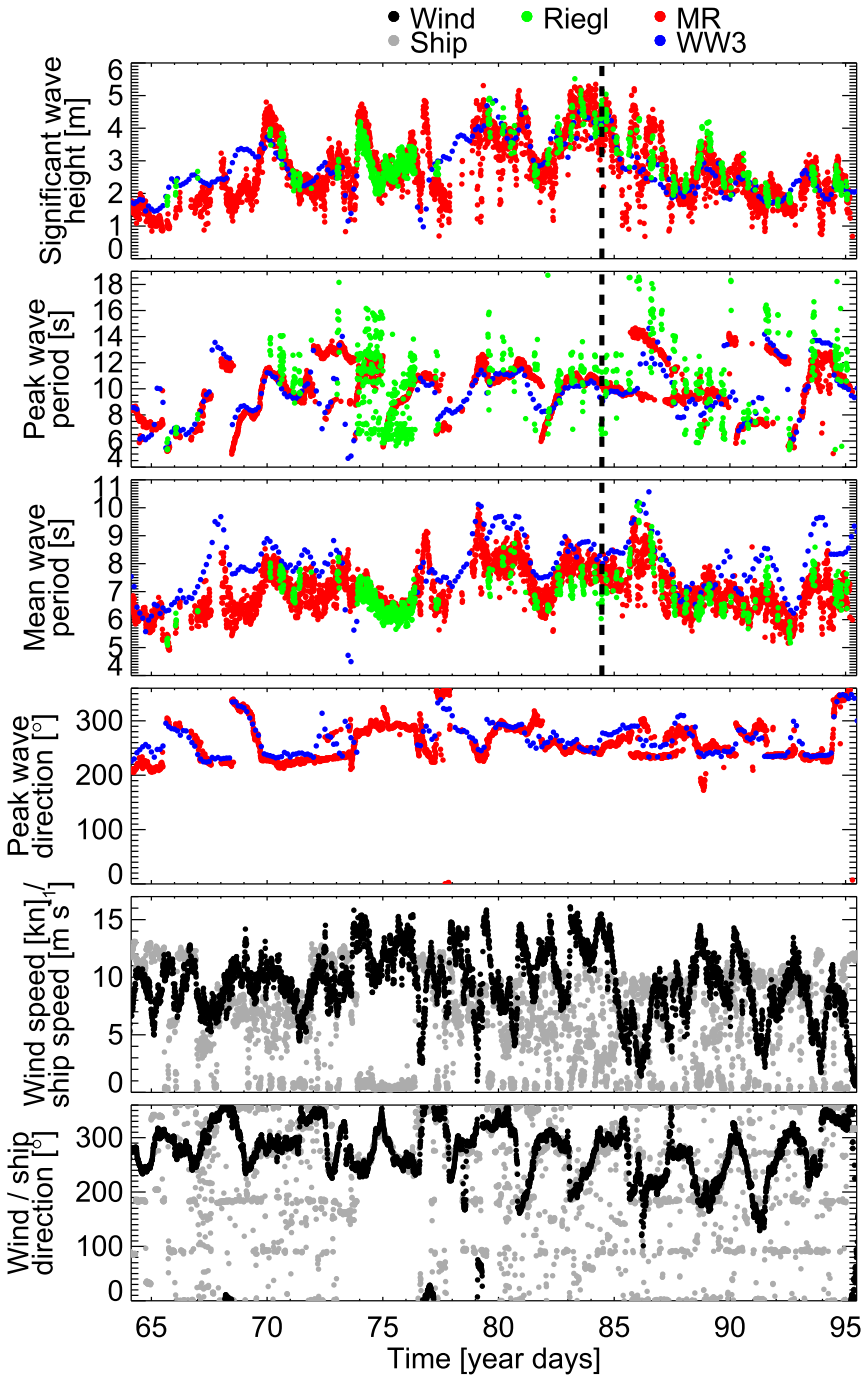


FIG. 9. Time series of MR (red), Riegl (green), and WW3 (blue) peak and integral wave parameters from *Ronald H. Brown* during SOGasEx. MR–Riegl (right) training and (left) testing datasets are indicated (dashed vertical line) in the top three panels. Corresponding wind measurements (black), and the ship's SOG and heading (gray), are shown in the bottom two panels.

within the shipboard MR frequency–direction spectra collected during SOGasEx. A training set of Riegl laser altimeter measurements was utilized to define a novel ETF that redistributes wave energy from the low to the high frequencies. The bias-corrected MR wave frequency spectra from both the training and testing datasets are in good agreement with the Riegl reference measurements. The high-frequency tails of both MR

Brought to you by NOAA Central Library | Unauthenticated | Downloaded 01/16/24 07:13 PM UTC

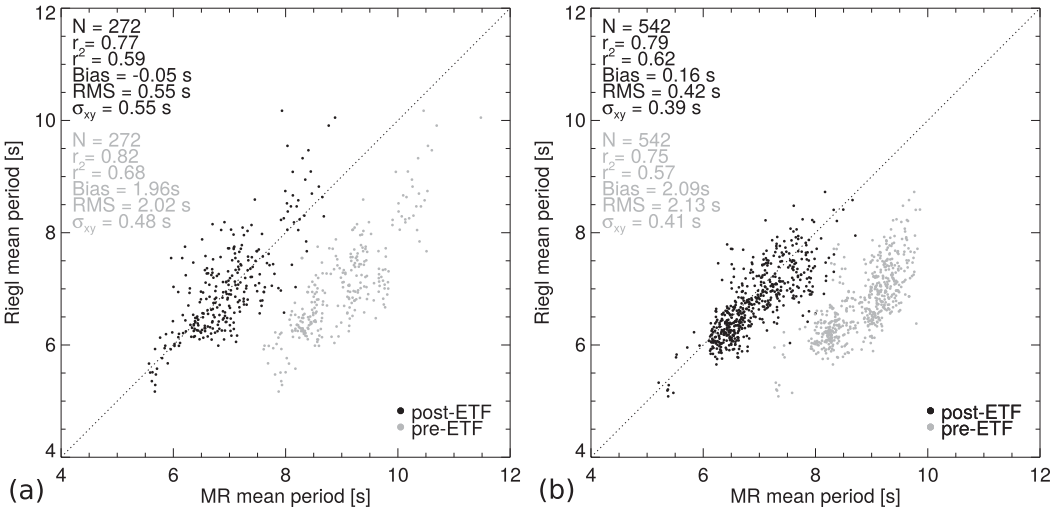


FIG. 10. Scatterplots of the pre-bias-correction (gray) and post-bias-correction (black) MR $T_{m01}$ measurements vs corresponding Riegl $T_{m01}$ measurements from the (a) training and (b) testing datasets.

and Riegl spectra follow the well-established $f^{-4}$ slope (Donelan et al. 1985). For the MR spectra, these observations hold true independent of ship motion. The MR wave frequency–direction spectra and Riegl frequency spectra furthermore agree reasonably well with the WW3 model results.

For optimal shipboard wave measurements, this study recommends combining MR with a secondary sensor that measures waves directly. Using a shipboard IMU paired with an altimeter is particularly compelling, since it allows sampling waves that are significantly shorter than the ship and it avoids the simplifying assumption that the ship responds to the wave field in the same way as a surface-following buoy (e.g., Collins et al. 2015). The MR benefits are twofold: 1) it provides the fully directional two-dimensional wave spectrum (i.e., no data-adaptive method is needed) and 2) its wave spectra can be accurate independent of ship motion. The laser altimeter measurements provide a reliable means of calibrating the MR $H_s$ and correcting shortcomings in the standard MTF by Nieto Borge et al. (2004). But at the moment, they can be used only during periods of near stationarity (with waves coming from the ship's forward section). In the future, it should be possible to Doppler correct altimeter wave records for ship motion, using MR wave frequency–direction spectra and near-surface current estimates as guidance. But given the strongly multimodal character of the observed Southern Ocean wave field, this requires an extension of the Doppler correction methodology proposed by Collins et al. (2016), who assumed the mean wave direction to be invariant with frequency and disregarded directional spread effects.

In the presence of heavy fog or rain, which can be easily detected using the zero-pixel percentage (Lund et al. 2012), the MR $H_s$ estimates are biased low. This is a weak point that could be addressed by replacing the MR estimate with its corresponding altimeter measurement. Alternatively, the standard SNR-based method could be replaced by one that exploits the shadowing in the MR backscatter images (Gangeskar 2014; Liu et al. 2016) or, if a coherent MR is available, by exploiting the Doppler

TABLE 1. MR and Riegl peak and integral wave parameter comparison statistics for the training and testing datasets. For $T_p$ and $T_{m01}$ the statistics prior to the ETF application are included as well. RMSE is the root-mean-square error and $N$ is the number of data pairs.

| | MR–Riegl (training) | | | | | MR–Riegl (testing) | | | | |
|---|---|---|---|---|---|---|---|---|---|---|
| | $H_s$ | $T_p$ | $T_{m01}$ | $T_p$ (pre-ETF) | $T_{m01}$ (pre-ETF) | $H_s$ | $T_p$ | $T_{m01}$ | $T_p$ (pre-ETF) | $T_{m01}$ (pre-ETF) |
| $r$ | 0.69 | 0.60 | 0.77 | 0.59 | 0.82 | 0.80 | 0.62 | 0.79 | 0.29 | 0.75 |
| $r^2$ | 0.48 | 0.35 | 0.59 | 0.35 | 0.68 | 0.64 | 0.39 | 0.62 | 0.09 | 0.57 |
| Bias | 0.00 m | −0.15 s | −0.05 s | 1.23 s | 1.96 s | 0.12 m | 0.71 s | 0.16 s | 1.82 s | 2.09 s |
| RMSE | 0.60 m | 2.34 s | 0.55 s | 2.65 s | 2.02 s | 0.52 m | 1.99 s | 0.42 s | 3.11 s | 2.13 s |
| $\sigma_{xy}$ | 0.60 m | 2.33 s | 0.55 s | 2.34 s | 0.48 s | 0.51 m | 1.85 s | 0.39 s | 2.52 s | 0.41 s |
| $N$ | 272 | 272 | 272 | 272 | 272 | 542 | 542 | 542 | 542 | 542 |

Brought to you by NOAA Central Library | Unauthenticated | Downloaded 01/16/24 07:13 PM UTC

signal associated with the wave orbital motion (Carrasco et al. 2017). Last, additional work is needed to assess the ETF used here under different wave environments (e.g., wind-sea-dominated seas or shallow coastal waters), with different MR parameters (e.g., antenna height and polarization) and data acquisition settings (e.g., an extended maximum range).

*Acknowledgments.* CJZ acknowledges funding by the National Science Foundation (Grants OCE-0647667 and OCE-1537890) and the National Oceanic and Atmospheric Administration (Grant NA07OAR4310094). BL and HCG acknowledge funding by the U.S. Office of Naval Research (Grants N00014-13-1-0288 and N00014-15-1-2638). WW3 results were generously provided by IFREMER through their comprehensive hindcast database (ftp://ftp.ifremer.fr/ifremer/ww3/HINDCAST). This is Lamont-Doherty Earth Observatory contribution number 8135.

## REFERENCES

Björkqvist, J.-V., H. Pettersson, L. Laakso, K. K. Kahma, H. Jokinen, and P. Kosloff, 2016: Removing low-frequency artefacts from Datawell DWR-G4 wave buoy measurements. *Geosci. Instrum. Methods Data Syst.*, **5**, 17–25, doi:10.5194/gi-5-17-2016.

Bourassa, M. A., and Coauthors, 2013: High-latitude ocean and sea ice surface fluxes: Challenges for climate research. *Bull. Amer. Meteor. Soc.*, **94**, 403–423, doi:10.1175/BAMS-D-11-00244.1.

Carrasco, R., M. Streßer, and J. Horstmann, 2017: A simple method for retrieving significant wave height from Dopplerized X-band radar. *Ocean Sci.*, **13**, 95–103, doi:10.5194/os-13-95-2017.

Cifuentes-Lorenzen, A., J. B. Edson, C. J. Zappa, and L. Bariteau, 2013: A multisensor comparison of ocean wave frequency spectra from a research vessel during the Southern Ocean Gas Exchange Experiment. *J. Atmos. Oceanic Technol.*, **30**, 2907–2925, doi:10.1175/JTECH-D-12-00181.1.

Collins, C. O., III, W. E. Rogers, A. Marchenko, and A. V. Babanin, 2015: In situ measurements of an energetic wave event in the Arctic marginal ice zone. *Geophys. Res. Lett.*, **42**, 1863–1870, doi:10.1002/2015GL063063.

——, and Coauthors, 2016: Doppler correction of wave frequency spectra measured by underway vessels. *J. Atmos. Oceanic Technol.*, **34**, 429–436, doi:10.1175/JTECH-D-16-0138.1.

Dittmer, J., 1995: Use of marine radars for real time wave field survey and speeding up transmission/processing. Proceedings of the WMO/IOC Workshop on Operational Ocean Monitoring Using Surface Based Radars, MMROA 32, WMO/TD-694, 133–137.

Donelan, M. A., J. Hamilton, and W. H. Hui, 1985: Directional spectra of wind-generated waves. *Philos. Trans. Roy. Soc. London*, **315A**, 509–562, doi:10.1098/rsta.1985.0054.

——, F. W. Dobson, S. D. Smith, and R. J. Anderson, 1993: On the dependence of sea surface roughness on wave development. *J. Phys. Oceanogr.*, **23**, 2143–2149, doi:10.1175/1520-0485(1993)023<2143:OTDOSS>2.0.CO;2.

Drennan, W. M., M. A. Donelan, N. Madsen, K. B. Katsaros, E. A. Terray, and C. N. Flagg, 1994: Directional wave spectra from a swath ship at sea. *J. Atmos. Oceanic Technol.*, **11**, 1109–1116, doi:10.1175/1520-0426(1994)011<1109:DWSFAS>2.0.CO;2.

Gangeskar, R., 2014: An algorithm for estimation of wave height from shadowing in X-band radar sea surface images. *IEEE Trans. Geosci. Remote Sens.*, **52**, 3373–3381, doi:10.1109/TGRS.2013.2272701.

Gemmrich, J., J. Thomson, W. E. Rogers, A. Pleskachevsky, and S. Lehner, 2016: Spatial characteristics of ocean surface waves. *Ocean Dyn.*, **66**, 1025–1035, doi:10.1007/s10236-016-0967-6.

Gille, S. T., 2002: Warming of the Southern Ocean since the 1950s. *Science*, **295**, 1275–1277, doi:10.1126/science.1065863.

Hanson, K. A., T. Hara, E. J. Bock, and A. B. Karachintsev, 1997: Estimation of directional surface wave spectra from a towed research catamaran. *J. Atmos. Oceanic Technol.*, **14**, 1467–1482, doi:10.1175/1520-0426(1997)014<1467:EODSWS>2.0.CO;2.

Hauser, D., K. K. Kahma, H. E. Krogstad, S. Lehner, J. Monbaliu, and L. R. Wyatt, Eds., 2005: Measuring and analysing the directional spectrum of ocean waves. COST Action 714, Office for Official Publications of the European Communities EUR 21367, 467 pp.

Hemer, M. A., J. A. Church, and J. R. Hunter, 2010: Variability and trends in the directional wave climate of the southern hemisphere. *Int. J. Climatol.*, **30**, 475–491, doi:10.1002/joc.1900.

Hessner, K. G., J. C. Nieto-Borge, and P. S. Bell, 2008: Nautical radar measurements in Europe: Applications of WaMoS II as a sensor for sea state, current and bathymetry. *Remote Sensing of the European Seas*, Springer, 435–446, doi:10.1007/978-1-4020-6772-3_33.

Ho, D. T., and Coauthors, 2011: Southern Ocean Gas Exchange Experiment: Setting the stage. *J. Geophys. Res.*, **116**, C00F08, doi:10.1029/2010JC006852.

Högström, U., E. Sahlée, A.-S. Smedman, A. Rutgersson, E. Nilsson, K. K. Kahma, and W. M. Drennan, 2015: Surface stress over the ocean in swell-dominated conditions during moderate winds. *J. Atmos. Sci.*, **72**, 4777–4795, doi:10.1175/JAS-D-15-0139.1.

Lindgren, G., I. Rychlik, and M. Prevosto, 1999: Stochastic Doppler shift and encountered wave period distributions in Gaussian waves. *Ocean Eng.*, **26**, 507–518, doi:10.1016/S0029-8018(98)00015-8.

Liu, X., W. Huang, and E. W. Gill, 2016: Comparison of wave height measurement algorithms for ship-borne X-band nautical radar. *Can. J. Remote Sens.*, **42**, 343–353, doi:10.1080/07038992.2016.1177450.

Lund, B., H. C. Graber, and R. Romeiser, 2012: Wind retrieval from shipborne nautical X-band radar data. *IEEE Trans. Geosci. Remote Sens.*, **50**, 3800–3811, doi:10.1109/TGRS.2012.2186457.

——, C. O. Collins III, H. C. Graber, E. Terrill, and T. H. C. Herbers, 2014: Marine radar ocean wave retrieval's dependency on range and azimuth. *Ocean Dyn.*, **64**, 999–1018, doi:10.1007/s10236-014-0725-6.

——, H. C. Graber, K. Hessner, and N. J. Williams, 2015a: On shipboard marine X-band radar near-surface current "calibration." *J. Atmos. Oceanic Technol.*, **32**, 1928–1944, doi:10.1175/JTECH-D-14-00175.1.

——, ——, H. Tamura, C. O. Collins III, and S. M. Varlamov, 2015b: A new technique for the retrieval of near-surface vertical current shear from marine X-band radar images. *J. Geophys. Res. Oceans*, **120**, 8466–8486, doi:10.1002/2015JC010961.

Brought to you by NOAA Central Library | Unauthenticated | Downloaded 01/16/24 07:13 PM UTC

——, C. O. I. Collins, H. Tamura, and H. C. Graber, 2016: Multidirectional wave spectra from marine X-band radar. *Ocean Dyn.*, **66**, 973–988, doi:10.1007/s10236-016-0961-z.

Nielsen, U. D., and D. C. Stredulinsky, 2012: Sea state estimation from an advancing ship —A comparative study using sea trial data. *Appl. Ocean Res.*, **34**, 33–44, doi:10.1016/j.apor.2011.11.001.

Nieto Borge, J. C., G. Rodríquez Rodríguez, K. Hessner, and P. Izquierdo González, 2004: Inversion of marine radar images for surface wave analysis. *J. Atmos. Oceanic Technol.*, **21**, 1291–1300, doi:10.1175/1520-0426(2004)021<1291:IOMRIF>2.0.CO;2.

——, K. Hessner, P. Jarabo-Amores, and D. de la Mata-Moya, 2008: Signal-to-noise ratio analysis to estimate ocean wave heights from X-band marine radar image time series. *IET Radar Sonar Navig.*, **2**, 35–41, doi:10.1049/iet-rsn:20070027.

Rascle, N., and F. Ardhuin, 2013: A global wave parameter database for geophysical applications. Part 2: Model validation with improved source term parameterization. *Ocean Modell.*, **70**, 174–188, doi:10.1016/j.ocemod.2012.12.001.

Riegl, 2010: LD90-3800-FLP data sheet. 2 pp., http://www.riegl.com/uploads/tx_pxpriegldownloads/10_29_DataSheet_LD90-3800-FLP_25-03-2010_01.pdf.

Sahlée, E., W. M. Drennan, H. Potter, and M. A. Rebozo, 2012: Waves and air-sea fluxes from a drifting ASIS buoy during the Southern Ocean Gas Exchange experiment. *J. Geophys. Res.*, **117**, C08003, doi:10.1029/2012JC008032.

Senet, C. M., J. Seemann, and F. Ziemer, 2001: The near-surface current velocity determined from image sequences of the sea surface. *IEEE Trans. Geosci. Remote Sens.*, **39**, 492–505, doi:10.1109/36.911108.

Sprintall, J., T. K. Chereskin, and C. Sweeney, 2012: High-resolution underway upper ocean and surface atmospheric observations in Drake Passage: Synergistic measurements for climate science. *Oceanography*, **25** (3), 70–81, doi:10.5670/oceanog.2012.77.

Stredulinsky, D. C., and E. M. Thornhill, 2011: Ship motion and wave radar data fusion for shipboard wave measurement. *J. Ship Res.*, **55**, 73–85.

Swail, V. R., and A. T. Cox, 2000: On the use of NCEP–NCAR reanalysis surface marine wind fields for a long-term North Atlantic wave hindcast. *J. Atmos. Oceanic Technol.*, **17**, 532–545, doi:10.1175/1520-0426(2000)017<0532:OTUONN>2.0.CO;2.

Wright, J., 1968: A new model for sea clutter. *IEEE Trans. Antennas Propag.*, **16**, 217–223, doi:10.1109/TAP.1968.1139147.

Young, I. R., 1999: Seasonal variability of the global ocean wind and wave climate. *Int. J. Climatol.*, **19**, 931–950, doi:10.1002/(SICI)1097-0088(199907)19:9<931::AID-JOC412>3.0.CO;2-O.

——, W. Rosenthal, and F. Ziemer, 1985: A three-dimensional analysis of marine radar images for the determination of ocean wave directionality and surface currents. *J. Geophys. Res.*, **90**, 1049–1059, doi:10.1029/JC090iC01p01049.

Zappa, C. J., W. E. Asher, and A. T. Jessup, 2001: Microscale wave breaking and air-water gas transfer. *J. Geophys. Res.*, **106**, 9385–9391, doi:10.1029/2000JC000262.

——, ——, ——, J. Klinke, and S. R. Long, 2004: Microbreaking and the enhancement of air-water transfer velocity. *J. Geophys. Res.*, **109**, C08S16, doi:10.1029/2003JC001897.

Ziemer, F., 1995: An instrument for the survey of the directionality of the ocean wave field. Proceedings of the WMO/IOC Workshop on Operational Ocean Monitoring Using Surface Based Radars, MMROA 32, WMO/TD-694, 81–87.

Brought to you by NOAA Central Library | Unauthenticated | Downloaded 01/16/24 07:13 PM UTC